Simulation Modelling Practice and Theory 132 (2024) 102881

Contents lists available at ScienceDirect

Simulation Modelling Practice and Theory

journal homepage: www.elsevier.com/locate/simpat

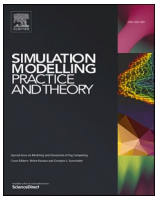

Digital Twin of the laser-DED process based on a multiscale approach

Sebastian Hartmann [a,c,1,*], Oihane Murua [b,1], Jon Iñaki Arrizubieta [b], Aitzol Lamikiz [b], Peter Mayr [a]

[a] Technical University of Munich, Materials Engineering of Additive Manufacturing, Munich, Germany
[b] Department of Mechanical Engineering, University of the Basque Country UPV/EHU, Bilbao, Spain
[c] Siemens AG, Erlangen, Germany

ARTICLE INFO

Keywords:
Digital Twin
Additive manufacturing
Physics-based simulation
Process monitoring
Directed energy deposition
Laser metal deposition

ABSTRACT

The ramp-up of new geometries, process parameters, and materials can be enormously time and cost-intensive in Additive Manufacturing. Especially for Laser-Directed Energy Deposition (DED-L), the extreme physical environment at the melt pool results in the need for multiple trial-and-error tests to quantify the process behavior. These tests significantly raise manufacturing expenses. A Digital Twin (DT) of the DED-L process can therefore be of substantial value if the amount of experimental testing is hereby reduced. In the present study, a multiscale DT based on coupling a global and local model has been investigated. The global model simulates the heating of the entire part, whereas the local model represents only a specific region of this global geometry. Using a high-density mesh for the local model enables the simulation of the specific laser-powder interactions and fast-cooling rates typical in DED-L. The results of the global model are used to integrate context awareness about the changing process conditions during the print job into the local model. This process evolvement is impossible to obtain with models of smaller dimensions and is of elemental necessity for accurately simulating multi-clad depositions. The DT was validated on an industrial-grade DED-L machine with in-situ process monitoring capabilities. In all cases, the DT shows a high resemblance with the experimental data and metallographic inspections at a reasonable computational cost.

1. Introduction

Additive Manufacturing (AM) enables the production of functional and complex parts in a resource-efficient way, applying only the required material where desired. The different AM processes hold the potential to initiate a fundamental change in the manufacturing industry [1]. Amongst these processes, especially Laser Directed Energy Deposition (DED-L) enables an excellent trade-off between production time and part complexity. By depositing metal powder onto a substrate in combination with a high-power laser, three-dimensional structures can be manufactured faster when compared to other metal AM processes [2]. Additionally, powder-based DED-L can be utilised to produce complex geometries with a wide range of materials that could not have been produced with any other technology [3]. Due to its unique advantages, DED-L has become an important technique in the production of high-performance parts

* Corresponding author at: Frauenauracher Straße 80 in 91056 Erlangen, Germany.
E-mail address: sebastian.m.hartmann@tum.de (S. Hartmann).
[1] These authors contributed equally to this work.

https://doi.org/10.1016/j.simpat.2023.102881
Received 29 August 2023; Received in revised form 6 December 2023; Accepted 14 December 2023
Available online 22 December 2023
1569-190X/Â© 2023 The Author(s). Published by Elsevier B.V. This is an open access article under the CC BY-NC-ND license (http://creativecommons.org/licenses/by-nc-nd/4.0/).

in the aerospace sector [4]. Coating and repair applications are also major drivers in the growing adoption of DED-L [5]. However, like all AM processes, this metal AM technology is currently lacking in process stability and quality of its final products. The complex physical phenomena involved in the laser-powder interaction as well as the cyclic thermal loading of the layer-wise manufacturing process can cause unexpected mechanical and geometrical properties [6]. The DED-L manufacturing uncertainties result in a demanding process parametrisation and often require multiple trial-and-error tests. Therefore, the implementation of computational models or Digital Twins (DT) are key elements to reduce those tests and obtain the first starting parameters.

A DT is a virtual model that represents the characteristics and behaviors of real physical systems, like a product, process, or machine. With the DT, the behavior of the physical system can be simulated and tested under different conditions. This leads to an enhanced understanding of its corresponding physical counterpart [7]. Experimental trial-and-error procedures can be diminished, resulting in reduced expenditures of both time and money [8]. The work of DebRoy et al. [9] laid the basis for the increasing adoption of DTs in the academic AM sphere. They first proposed to utilize DTs to reduce the extensive trial and error cycles that are deeply linked with AM at present. Since the initial work of DebRoy et al., multiple research efforts have been published in the field of DTs in AM. Gaikwad et al. [10] presented a machine learning framework that combines a physical simulation with in-situ sensor data. They proved that the predictive capability of a DT increases once simulated and real process data are combined in one framework. Gunasegaram et al. [11] further expressed the need to create physically validated process models capable of predicting the outcome of the real process. The authors specifically pointed out that the validation of the developed DT is crucial for its reliable predictive capabilities. Mukherjee and DebRoy [12] emphasized the need for an accurate mechanistic simulative model, and they defined the results that such a simulation model should be able to predict. Moreover, Reisch et al. [13] proposed a spatial-context-aware DT for Wire Arc Additive Manufacturing (WAAM). Data streams from multiple sensors were collected and fused with the respective Tool Centre Points during the production process. Hereby, spatial awareness of the DT was created, enabling a more sophisticated analysis of the spatial correlation between single defects inside of a part. In DED-L, the work of Hermann et al. [14] established the first combination of data-driven and physical simulation models in a DT. Nevertheless, the machine learning algorithms and DTs were used solely for the prediction of the geometry of single tracks.

According to Soares do Amaral et al. [15], the simulation of a complex system can be defined in multiple ways. Examples are the finite element method, finite difference method, Gipps' model, discrete event simulation, agent-based simulation, and Monte Carlo simulation, among others. However, numerical methods based on solving the differential equations are the most common approach thanks to the flexibility they offer. The numerical simulation of the DED-L process has already been the focus of multiple scientific efforts. Arrizubieta et al. [16] investigated the influence of melt pool fluid dynamics on the predictive accuracy of the DED-L process. The simulation model was validated by comparing its results with the temperature of the melt pool, measured with a pyrometer, and the dimensions of cross-sectioned parts of the deposited clads. The model was able to predict the deposited clad geometries of the DED-L process with an error below 10%, and it was concluded that there is no need to consider the melt pool dynamics in the powder-based DED-L process. However, the model presented limitations in terms of part size and the associated computational cost, which restricted its use to small geometries. Ling et al. [17] combined a finite element model with a neural network to accurately predict the hardness and ultimate strength of the later part produced with WAAM. Multiple process parameters were varied, and the model accuracy was obtained for every parameter set, resulting in errors close to 0%.

Using graph theory thermal modelling, Riensche et al. [18] pointed out that the thermal history of a DED-L part can be simulated rapidly. The temperature measurements were collected with two thermocouples embedded inside of the printed substrates. Nevertheless, the model was not capable of predicting the clad geometry, and the width and height were considered as input parameters. The same assumption is also considered by many DTs aimed at the Powder Bed Fusion (PBF) process, in which the clad height is known beforehand [19]. However, this approach to reduce the computational cost is not valid for the DED-L process, where the clad dimensions vary depending on the process parameters and the evolution of the thermal field. Another alternative to reduce the computational cost of the simulation is the use of analytical or semi-analytical models. For example, Weisz-Patrault [20] presented a semi-analytical tool to simulate temperature evolutions and phase transitions during DED-L. The developed tool enables a faster computational time with an average error of 2.6% for the studied situations but also neglects multiple process phenomena. Consequently, the model was only developed and validated for axisymmetric or 2D geometries, which is a clear limitation for real process situations. In order to reduce the computational cost of the models, multiscale approaches have also been considered. For instance, Yan et al. [21] presented a roadmap for developing multi-physics multiscale process models and mechanistic models that simulate the manufacturing process of the DED-L process, but no validation procedure or experimental data was provided.

Considering the importance of a proper validation of the model, the use of monitoring and sensing systems is common for obtaining experimental data. The works of Tang et al. [22] and Liu et al. [23] summarise this vast field of different sensor systems and monitoring techniques that have already been investigated for DED-L. It can be stated, that in general, the melt pool remains the most essential characteristic to be monitored during the DED-L process [22]. On that note, He et al. [24] provided a comprehensive review about utilizing optical systems for in-situ monitoring of the melt pool during DED-L. They summarised the most important techniques and hardware systems to capture the essential melt pool information.

Once the latest advances in DTs for the DED-L process have been studied, it is clear that obtaining an accurate model that considers the clad generation and calculates the resulting thermal field in complex geometries at a relatively low computational cost is a milestone still to be achieved. In view of the necessity of developing a computationally optimised DT, in the present research, a multiscale approach is proposed and the model is validated through experimentally obtained data. In the local model, the clad geometry is defined based on the melt pool created by the laser beam and the powder distribution at the DED-L head exit. A dynamic meshing algorithm that modifies the node's position across time and adapts the geometry to the actual deposited clad is employed. In the global model, the thermal field of the whole part is simulated and the resulting geometry is obtained for the programmed machine

trajectories and parameters. Initially, the DT is validated for single clads with different process conditions and later for more complex process situations.

2. Methodology

The development of a Digital Twin (DT) is a complex task, where the experimental calibration and the posterior validation play an important role. Therefore, the characteristics of the machine to be used in the experimental setup and the material properties are essential. In order to achieve the proposed objective, first, the DT is applied to simple geometries, such as individual clads, and afterwards, it is employed for sharp edge deposition and multilayer strategies.

In the developed DT, the heat and material transfer problems are solved in a coupled way. The PDE toolbox of the Matlab R2023a software is employed, and the multiscale model is composed of a local and a global model. The aim of developing a multiscale DT is to reduce the computational cost, but without compromising the accuracy of the results. As the DT ought to be industrially applicable, having a low computational cost is a required characteristic. First, the local model is calibrated and validated through depositing simple geometries, such as single clads. For this purpose, the single clads are evaluated by metallographic inspection and the in-process melt-pool monitoring, and the obtained values are compared with those provided by the local model of the DT. Afterwards, the global model, which is aimed at simulating the overall DED-L process, is validated by measuring the temperatures in the base plate during the manufacturing process and correlating these values with the heat accumulation predicted by the global model of the DT. Moreover, the resulting geometry of the DT and the experimental tests are compared.

3. Model basis

The following section describes the model basis in detail. In general terms, the developed DT solves the thermal problem during the DED-L process, obtaining the thermal field based not only on the material properties but also on the machine characteristics. These heat and material transfer problems are solved by means of the PDE toolbox of the software Matlab.

3.1. Multiscale strategy of the DT

The multiscale model aims to solve the DED-L manufacturing process simulations by means of a fully coupled double model. Multiscale methods are considering different levels of complexity and detail of the underlying process while also coupling methods for its simulation [25]. The reason for this coupling is to obtain an accurate result at the lowest computational cost. The strategy of the

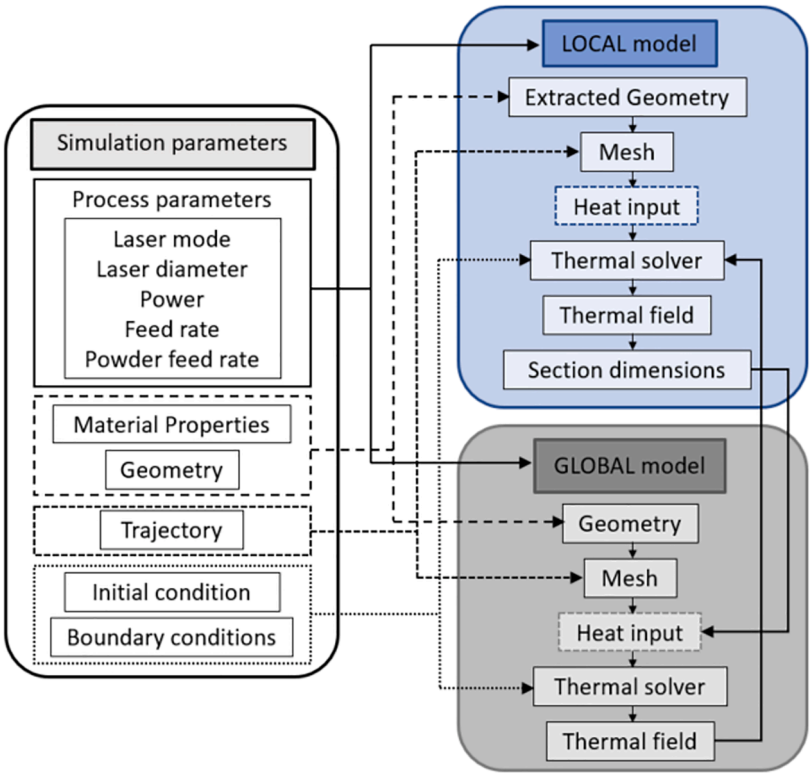

Fig. 1. The model strategy for the DED-L simulations.

multiscale model is to split the problem resolution into two steps, which helps to overcome the difficulties of solving the DED-L process in real-scale situations. Therefore, the implemented strategy is a combination of the local and global model resolutions, through which the respective scale problem is solved.

As it is represented in Fig. 1, the model is initialised by establishing the simulation parameters. The process parameters represent the main variables of the DED-L process, such as the laser characteristics and the powder, among others. Besides, the material properties and the initial geometry with its respective trajectory are also essential and need to be defined before running the simulation, together with the initial and boundary conditions.

After having all the simulation parameters defined, the global model is launched, where the whole geometry and trajectory are defined. However, in order to calculate the clad geometry and melt pool temperatures, a portion of the global mesh is extracted, and the local model is executed in it. This approach enables to refine the mesh and use smaller elements in the area where the laser beam irradiates the part. Once the local model is solved, the clad geometry and temperatures are obtained and exported to the global model. In a second step, the global model reconstructs the whole clad based on the programmed trajectory and by using the Delaunay triangulation algorithm. Besides, the heat introduced into the workpiece by the laser is simulated to account for the heat accumulation.

3.2. Assumptions

The assumptions considered to develop the DT at a reduced computational cost are listed below:

- In powder-based L-DED the melt pool flow is constantly disturbed by the impinging powder particles [26], and hence, the molten material presents a chaotic behavior with no preferred direction [27]. Therefore, in the present work melt pool dynamics are neglected in order to reduce computational cost. This assumption has also been considered in previous works and yielded accurate results [20,28].
- The material vaporization is ignored, as this phase change of the material is not expected to occur in the DED-L. This assumption is typical for models which are meant to reproduce operational simulations.
- The laser beam attenuation due to the powder shadow is neglected. The model considers that the heat attenuated by the powder particles is absorbed by them and therefore, introduced again into the system once the particles are injected into the melt pool.
- All filler material that falls inside the melt pool is considered to become part of the clad, whereas the powder that falls outside the melt pool is considered to bounce off on the solid surface and is assumed to be lost.
- The material properties are considered to be temperature dependent.
- The composition of the material within the clad is assumed to be constant. Based on the low dilution of the clad, the composition is considered to be that of the filler material [29].
- The absorptivity of nickel-based alloys is measured between 0.3 and 0.7 [30,31]. Employing constant values close to 0.37 is common for fiber lasers when working with Inconel 625 as a bulk material [32]. In the present work, the absorptivity coefficient is determined to adjust the model and the experimental results. A constant value of 0.35 is considered appropriate for the employed configuration. This value is also in accordance with the findings of Liu et al. [33] and Lia et al. [34].

3.3. Thermal model

The thermal model is developed by implementing the Finite Element Method (FEM), which leads to simplifying the resolution of complex problems. The thermal field resolution is focused on solving the partial derivative heat transfer equation (Eq. (1)) by employing the Matlab PDE toolbox, where ρ [kg·m^{-3}] is the density of the material, C_p [J·kg^{-1}·°C^{-1}] is the specific heat, k [W·m^{-1}·°C^{-1}] is the thermal conductivity, T [°C] is the temperature, and f [W·m^{-2}] is the heat generated by the laser:

$$\rho \cdot C_p \cdot \frac{\partial T}{\partial t} - \nabla \cdot (k \cdot \nabla T) = f \tag{1}$$

This equation is evaluated in the local and global model. In the case of the local model, a circular-shaped laser beam is modelled as the heat input, see Section 3.6. However, in the global model, the whole clad is simulated at once, and therefore, the laser heat is distributed in the entire area and averaged during the total time required for the clad deposition.

3.4. Trajectory

The laser path is defined by the user depending on the geometry desired to be built. Therefore, the user determines the fixed points through which the laser will pass, and afterwards, the model unites these points with straight lines and discretizes the lines based on the defined step. For the present case, a 1 mm spatial discretization is used for the trajectory vector. The trajectory matrix $[P(t)]$ is formed by 8 columns, as it is represented in Eq. (2). The first three columns correspond to the XYZ coordinates of the DED-L head and the 4th and 5th columns represent the A and B rotation movements, corresponding to the X and Y axes respectively. The 6th column represents the laser power, and the 7th is the feed rate. Finally, the 8th column contains the amount of time that the DED-L head stays on every single point of the trajectory matrix. The 8th column value is defined by Eq. (3), where t stands for a determined time instant and $t+1$ is the subsequent one.

$$[P(t)] = [\{P(1,t)\}\{P(2,t)\}\ \{P(3,t)\}\ \{P(4,t)\}\ \{P(5,t)\}\ \{P(6,t)\}\ \{P(7,t)\}\{P(8,t)\}] \tag{2}$$

$$\{P(8,t)\} = \left(\sum_{i=1}^{3}(\{P(i,t+1)\} - \{P(i,t)\})^2\right)^{1/2} \cdot \{P(7,t)\}^{-1} \tag{3}$$

The trajectory matrix is employed during the simulations, henceforth when the laser power changes from a positive value to zero, the laser is automatically switched off, as in the opposite case. Thereby, this matrix resembles the CNC mechanism operating the DED-L machine.

3.5. Initial conditions

Regarding the necessity of initial conditions for the model simulation, the initial temperature, T_0, is set in the full domain of the simulations, where Ω is the evaluation domain and u is the position vector, $\{u\} = \{x,y,z\}\ \forall\Omega$. For the initial instant t=0 the temperature is determined by the user, see Eq. (4). However, for the next steps the temperature is linearly interpolated from the thermal field at the end of the previous steps. For the current simulations, the initial temperature is set at 25°C, which has been measured experimentally prior to the tests.

$$\begin{aligned} \{T_0(\{u\},0)\} &= 25^{\circ}C \\ \{T_0(\{u\},t+1)\} &= \{\widehat{T}(\{u\},t)\} \end{aligned} \tag{4}$$

3.6. Boundary conditions

The boundary conditions, BC, are divided along the geometry in order to represent the real behavior of the part. Three BCs are defined; the first one, Γ_1, corresponds to the area the laser beam irradiates, the second one, Γ_2, refers to the external faces of the geometry except for the lowest face, and the third one, Γ_3, represents the contact with the machine table at the lower face of the full geometry. In Fig. 2, the BCs applied in the DT are summarized.

The laser beam is modelled differently in each model. On the one hand, knowing that the employed laser, YLR-2000 from IPG Photonics, is an Ytterbium fiber laser, in the local model the beam is shaped as a top-hat heat source at the focal plane. This approach is grounded by the work carried out by Kubiak et al., who concluded that for Yb:YAG lasers the transversal energy mode approximates a top-hat distribution at the focal position [35]. In Eq. (5), the top-hat energy distribution is represented where α *[-]* is the absorptivity, P *[W]* is the time-dependent laser power, R *[mm]* is the laser beam radius, $\delta_{defocus}$ *[mm]* the laser defocus distance and φ *[°]* is the laser beam divergence angle.

$$f(\{u\},t) = \frac{\alpha \cdot \{P(6,t)\}}{\pi \cdot \left(R + \delta_{defocus}(\{u\}) \cdot tg(\varphi(\{u\}))\right)^2} \quad \in \Gamma_1 \tag{5}$$

On the other hand, in the global model, the laser beam is modelled as a uniform heat source along the deposited clad. This heat source is equivalent to the energy density applied during the clad deposition, which has the full clad shape and is active during the path deposition time. Eq. (6) represents the laser heat input for the global model where t_1 *[s]* is the initial time for the clad deposition, t_2 *[s]* is the final time, α is the absorptivity, and P is the time-dependent laser power. Lastly, A *[mm²]* is the area where the laser heat is introduced and is defined in Eq. (7).

$$f(\{u\},t) = \frac{\alpha \int_{t_1}^{t_2} \{P(6,t)\}dt}{A} \quad \in \Gamma_1 \tag{6}$$

$$A = \sum_{i=1}^{2} \frac{\pi R(t_i)^2}{2} + 2\int_{t_1}^{t_2} R(t)\{P(7,t)\}dt \tag{7}$$

The second boundary condition is applied to all external faces except the one in contact with the machine table. All these faces experience heat losses due to convection and radiation. For that reason, in Eq. (8), these losses are considered, where h_c *[W·m⁻²]* is the convection coefficient, ε *[-]* is the radiative emittance, and σ is the Stefan-Boltzmann constant ($5.67{\cdot}10^{-8}$ W·m^{-2}·K^{-4}). The employed coefficient values are listed in Table 2, where the convection coefficient has a 10 W·m^{-1}·K^{-1} value [36] and the radiative emittance

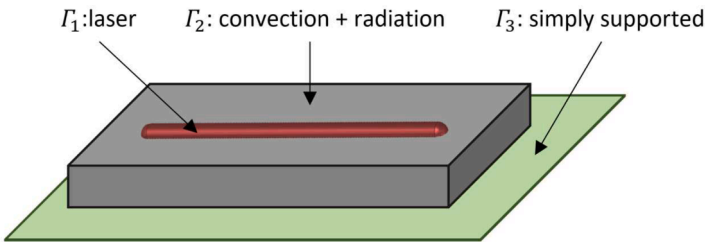

Fig. 2. Boundary conditions in the global model.

takes the same value as the absorptivity based on Kirchhoff's law of thermal radiation.

$$f(\{u\},t) = -h_c \cdot (T(\{u\},t) - T_{room}) - \varepsilon \cdot \sigma \cdot \left(T(\{u\},t)^4 - T_{room}^4\right) \in \Gamma_2 \tag{8}$$

Regarding the third and last BC, the modelled geometry is simply supported at the lower face by the machine table. Therefore, during the deposition process, conduction is allowed between the lower face of the part and the machine table. However, the big size of the machine table and the high thermal inertia imply that the temperature of the table hardly varies. Therefore, the lower face is assumed to have a constant room temperature, Eq. (9). In the present study, the room temperature is the same as the initial temperature, which is, 25°C.

$$T(\{u\},t) = T_{room} \in \Gamma_3 \tag{9}$$

3.7. Material addition

The material addition is calculated in the local model, where the thermal field generated by the laser beam absorption and the powder distribution at the DED-L head are combined in order to build a clad.

3.7.1. Local model

The strategy for the material addition is based on calculating the movement of the mesh nodes. The material is added to all nodes that have a temperature higher than the melting temperature, and their position is displaced accordingly, see Fig. 3. This means that the powder falling inside the melt pool is contributing to the clad construction, whereas the powder falling outside is lost.

In powder-based DED-L processes, the powder flow has a typical Gaussian distribution, where the maximum concentration is located at the axis center. Therefore, the nodes of the elements where the powder is injected are displaced according to Eq. (10), where M is the filler material mass rate, ρ_p is the density of the filler material at the given temperature (T_p) and R_p is the radius of the powder flow at the focal plane of the laser.

$$\begin{aligned}
\{d(\{u(1)\},t)\} &= \frac{2 \cdot M \cdot dt}{\rho_p(T_p) \cdot \pi \cdot R_p^2} \cdot e^{-2 \cdot \left(\frac{\{dp(2,t)\}^2 + \{dp(3,t)\}^2}{R_p^2}\right)} \cdot \sin(\{P(5,t)\}) \\
\{d(\{u(2)\},t)\} &= \frac{2 \cdot M \cdot dt}{\rho_p(T_p) \cdot \pi \cdot R_p^2} \cdot e^{-2 \cdot \left(\frac{\{dp(1,t)\}^2 + \{dp(3,t)\}^2}{R_p^2}\right)} \cdot \sin(\{P(4,t)\}) \\
\{d(\{u(3)\},t)\} &= \frac{2 \cdot M \cdot dt}{\rho_p(T_p) \cdot \pi \cdot R_p^2} \cdot e^{-2 \cdot \left(\frac{\{dp(1,t)\}^2 + \{dp(2,t)\}^2}{R_p^2}\right)} \cdot \cos(\{P(4,t)\}) \cdot \cos(\{P(5,t)\})
\end{aligned} \tag{10}$$

In Eq. (10) the variable dp represents the distance between the nodes $\{u(i)\}$ of the mesh and the laser position, for the X, Y, and Z axis, i=1:3, respectively.

$$\{dp(i,t)\} = \{u(i)\} - \{P(i,t)\} \;/\; i = 1:3 \tag{11}$$

Once the x, y, and z displacements have been obtained, the total displacement of the nodes in the local mesh is obtained, Eq. (12), and the new mesh can be defined according to Eq. (13).

$$d(\{u\},t) = [\{d(\{u(1)\},t)\};\ \{d(\{u(2)\},t)\};\ \{d(\{u(3)\},t)\}] \tag{12}$$

$$\Omega(\{u\},t+1) = \Omega(\{u\},t) + d(\{u\},t) \tag{13}$$

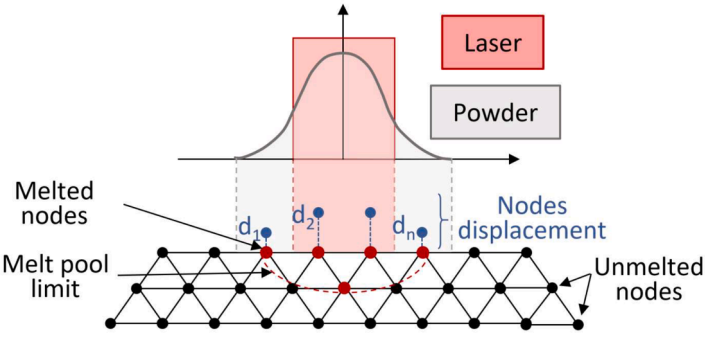

Fig. 3. Material addition process in the local model.

3.7.2. Global model

The dimensions of the clad obtained in the local model are exported to the global model, see Fig. 1. The global model creates a rectangular parallelepiped in each discretized position of the laser beam across the trajectory matrix, $[P(1:3,t)]$, and a point cloud is defined with all the vertexes. Notice that each parallelepiped width and height correspond to those of the clad calculated in the local model. Afterwards, duplicated points are deleted, and the point cloud is connected using Delaunay triangulation, see Fig. 4(a). This allows to define the new domain, $\Omega(\{u\}, t+1)$. The new geometry, including the generated clad is shown in Fig. 4(b).

During the global model resolution, the thermal field is calculated by means of solving the thermal transient equation (Eq. (1)). The introduced laser heat source is equivalent to the energy applied for the clad deposition. Thereby, the thermal field resolution in the global model is conducted by considering the clad dimensions obtained in the local model, with the aim of simulating the heat accumulation in the workpiece. Because of the automatic re-meshing between successive clads, the initial nodal temperatures are defined by employing an interpolating function based on the nodal temperatures of the previous step.

3.8. Mesh

When applying finite element methods, geometry discretization through meshing is a highly validated approach. In this case, it is constructed by first-order tetrahedral elements to avoid calculation instabilities due to the high thermal gradients present in the DED-L process. The convergence of the results was verified in the preliminary simulations, and a 0.2 mm minimum element size is identified as necessary to ensure the accuracy of the results, but without excessively increasing the computational cost.

The model calculation is eased by implementing an adaptive element size in the area where higher temperature gradients are expected, such as the area where the laser impacts. The global model simulates the whole part geometry, whereas the local model represents only a region of the global geometry. In Fig. 5, both meshes are shown, and the geometry extraction is represented. Employed element sizes are detailed in Table 2, where the parameters of the simulations, including the parameters of the machine itself, are listed. The mesh is updated in every step in order to adapt to the evolving geometry and avoid excessive element deformations.

4. Monitoring framework

For validating the numerical results of the DT, three sensor systems are deployed to monitor the predicted process parameters. First, the melt pool temperature and width are measured by an infrared, IR, camera, and a CMOS camera, respectively. The base plate temperature evolution is monitored by means of a thermocouple.

For the experiments, the IR camera PI05M from the company Optris GmbH was used to capture the melt pool temperature. It has a measurement range from 900°C to 2450°C and records a maximum of 80 frames per second. As an output value, the infrared camera provides the hottest pixel temperature within a predefined measuring field. The estimation of error for the IR measurements amounts to ± 1.5%. This measurement error is provided by the IR camera provider and is in accordance with the calibration tests performed prior to the actual experiments [37].

In addition to the temperature, the melt pool width is analyzed with a CMOS camera. The acA1300-75-gm from Basler AG is mounted in the optical path of the nozzle system by using a dichroic beam splitter and can capture up to 88 frames per second in greyscale. A schematic front view of the setup is shown in Fig. 6(b). The obtained images are analyzed with a self-developed Python code. At first, the images are binarized with a threshold value of 250, meaning that all pixels with a brightness of less than 250 are

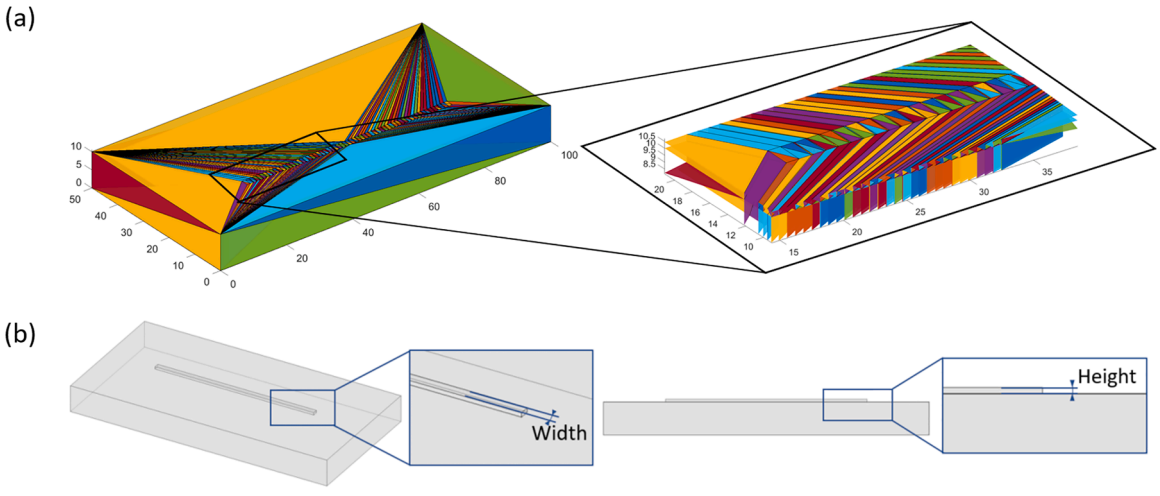

Fig. 4. (a) Delaunay triangulation for the geometry reconstruction in the global model after a clad is deposited, where a bright color palette is employed to facilitate the visual differentiation of the tetrahedrons, and (b) the resulting clad geometry in the global model.

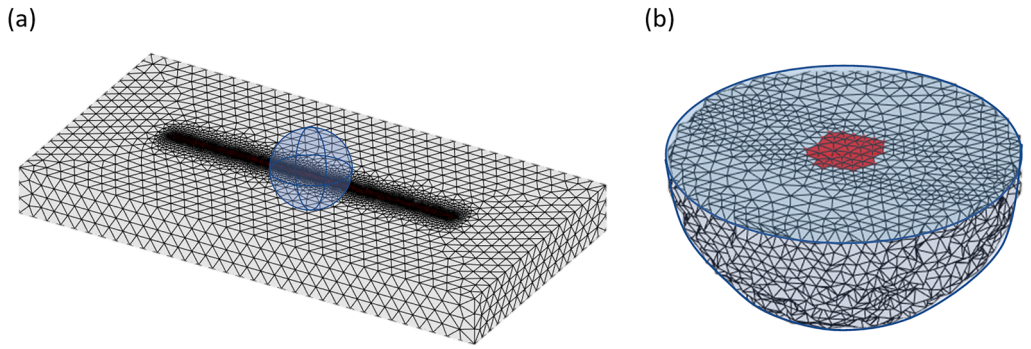

Fig. 5. The mesh configuration in the (a) global and (b) local model.

blacked. The threshold value is derived from Murua et al. [38], who developed a similar image-processing algorithm. In the next step, the Open Source Computer Vision library cv2 is utilized for detecting the edges of the remaining pixels. Therefore, depending on the orientation of the movement direction of the melt pool, the maximum detected edges of the melt pool is calculated.

The final metric to validate the DT is the temperature evolution of the base plate at a constant position, which measures the heat accumulation in the part. To monitor the temperature, a type K thermocouple in a sheath with a diameter of 1 mm was mounted at the same fixed position during each experimental run. The thermocouple, with the product number TK-M-G2-1.0-1100, from Sensorox GmbH & Co. KG was grounded and its position can be seen in Fig. 9 for all experiments. Its measuring range is between -220°C to 1150°C, and therefore, it was positioned relatively far from the melting region to avoid damage and reduce noise in the measurements [39]. During the initial tests, different positions of the thermocouple were tested to minimize the noise in the temperature data during the printing process.

After the final position was selected, more tests were done to validate the thermocouple's thermal responsivity. During these tests, base plates were pre-heated, and their respective surface temperature was measured with the employed thermocouple. The resulting measurement error was ±1.5°C which is in accordance with the acceptable limits defined for type K thermocouples by ASTM E230/E230M-17 (Standard Specification and Temperature-Electromotive Force Tables for Standardized Thermocouples). In all experiments, a clamping device, pressing the thermocouple to the part surface, was employed. Additionally, thermal grease was used to encase the thermocouple for a facilitated dissipation of heat from the base plate's surface.

The monitoring system is integrated into a BeAM Modulo 400 DED-L system. The BeAM machine is equipped with a SINUMERIK ONE numerical control unit and includes a 2 kW continuous maximum power Ytterbium fiber laser from IPG Photonics, model YLR-2000. The DED-L system has a build volume of 400 × 400 × 400 mm^3 and enables the production with two deposition heads. The positioning of the infrared camera is derived from Khanzadeh et al. [40]. The infrared camera is aligned with the center point of the mounted base plate. The distance between the center of the infrared optic and the middle of the base plate amounted to 25 cm. The angle between the center of the infrared optics and the center of the laser beam was approximately 45°. Different positions have been evaluated prior to the experiments, with the final position having the best trade-off between minimum distance and maximum optical coverage. The entire monitoring setup can be seen in Fig. 6.

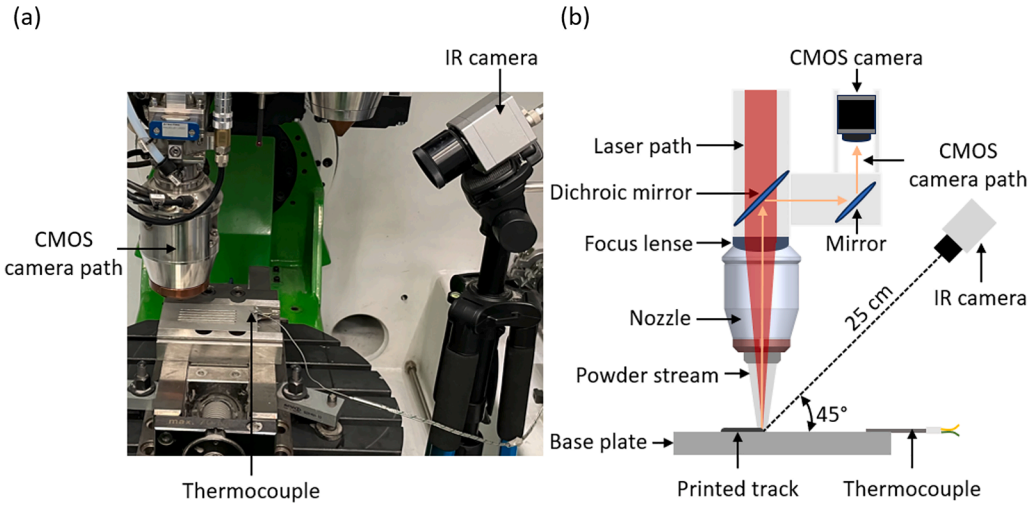

Fig. 6. Monitoring setup: (a) employed sensor systems inside of the building chamber, and (b) schematic front-view of the monitoring setup.

For a more comprehensive dataset, the sensor data is fused with the machine data points. From the numerical control of the machine, the exact positions of the Tool Centre Point, TCP, the real feed rates as well as the laser power have been collected. A Linux-based Edge IPC is employed to collect the data from the machine and the thermocouple in high frequency. The data from the CMOS camera, capturing the melt pool, and the infrared camera are collected on a Windows IPC. The appendix contains all data points and their respective frequencies that have been monitored and collected for the validation of the DT. To fuse all data points, one common frequency is defined. The frequency of the slowest system, the infrared camera, is chosen to be the overarching frequency for all data points. As a result, all sensor data points can be traced back to their specific location and spatial analytics of the sensor data are achieved. An example of this geomapping approach of the melt pool, MP, width data (in mm) can be seen in Fig. 7.

5. Experimental test planning and materials

5.1. Material specifications

In all the experimental tests, the same base material is used, which is the stainless steel 304 (SS304). The dimensions of the employed base plates are $100 \times 50 \times 10$ mm^{3,} and they have been grinded and cleaned before the deposition tests to ensure the same surface conditions in all cases. The powder material employed during the DED-L process is Inconel 625 (In625). The powder is gas atomised with a grainsize between 45 μm and 60 μm. The chemical compositions of both materials are displayed in Table 1.

The thermophysical properties of SS304 and Inconel 625 introduced in the model are temperature dependent, as it is shown in Fig. 8. The diagrams show the thermal conductivity, density, and specific heat of SS304 and Inconel 625 for the temperature range from 0 – 1000°C. In case of having higher temperatures, the properties are linearly extrapolated.

In Table 2, the simulation parameters defined in the DT are detailed. In case different values are employed in the global and local models, the corresponding numbers are provided. As indicated in Section 3.2., the absorptivity value is defined to fit the model with the experimental results, whereas the rest of the parameters (laser radius, powder flow, …) are taken from the real machine data.

5.2. Design of experiments

To validate the capabilities of the DT, a total of four experiments are defined. An overview of the printed geometries can be seen in Fig. 9.

- Experiments 1 and 2 consist of five consecutive single-tracks with a five millimetre distance in between. In both experiments, the same process parameters are employed, but the void movement velocity is modified (Fig. 9(a)). The void movement velocity stands for the velocity of the nozzle while the laser is turned off.
- Next to the standard single-track geometries, a U-shape clad is simulated in experiment 3 (Fig. 9(b)). The aim of this third experiment is to analyse the direction change region since corner sections are known as the most error-prone areas in DED-L parts, especially in terms of dimensional accuracy [47].
- Finally, in Experiment 4 (Fig. 9(c)), a single-track wall consisting of five layers is considered to study the capability of the model to simulate overlapping clad conditions.

In Experiments 1 and 2, the objective is to validate the capability of the DT for predicting the deposited clad height and width. For this purpose, the melt pool width measured by the CMOS camera as well as the experimental cross-sections of the individual clads are employed. The maximum temperature predicted by the DT is also compared with the IR camera measurement, and the cooling rate is validated by means of the secondary dendrite arm spacing (SDAS). The studied process parameters are the laser power, P, the velocity of the TCP (F), and the velocity during the transition movements with the laser off (F_0), see Table 3. Regarding the nomenclature, for instance the clad 1.2 stands for the second clad of the first experiment. The only difference between Experiments 1 and 2 is the F_0 velocity. Hereby, the effect of this parameter on the temperature evolution of the baseplate, measured with the thermocouple, can be investigated.

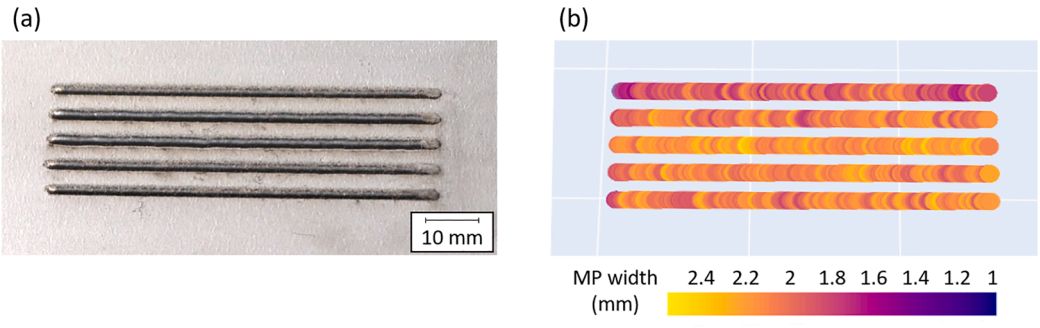

Fig. 7. Comparison between the (a) real process part and (b) the geomapping of the sensor data.

Table 1
Chemical composition of SS304 [41] and In625 (wt.%) [42].

Material	C	Cr	Ni	Fe	Mn	Si	P	S	N	Mo	Nb+Ta	Ti	Al	Oth.
SS304	0.07	18.0	9.0	Bal	2.0	1.0	0.045	0.015	0.1					
In625		21	Bal.	<5.0						9.0	4.0	0.4	0.4	<0.5

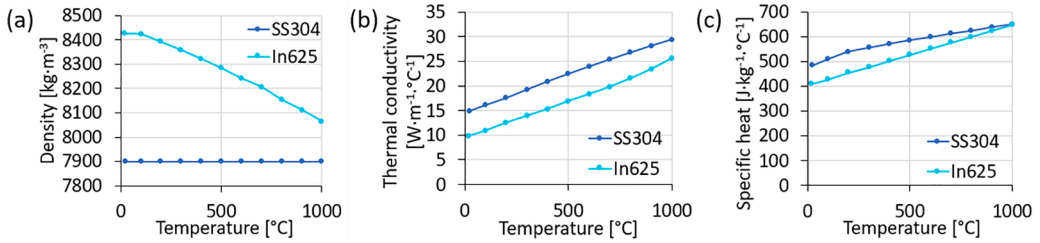

Fig. 8. Temperature-dependent material properties of SS304 and In625: (a) density [43,44], (b) thermal conductivity [45,46], and (c) specific heat [45,46].

Table 2
Simulation parameters in the DT.

Parameter	Unit	Value	
		Local Model	Global Model
Absorptivity (α)	[-]	0.35	
Element size (max, min)	[mm]	(1, 0.2)	(2, 0.4)
Mesh growth rate	[-]	1.1	
Trajectory discretisation step (Δu)	[mm]	0.2	1
Laser beam divergence angle (φ)	[°]	6.18	
Laser radius (R)	[mm]	1.2	
Convection coefficient (h_c) [36]	[W·m^{-2}]	10	
Radiative emittance (ε)	[-]	0.35	
Room temperature (T_{room})	[°C]	25	
Powder flow radius (R_p)	[mm]	1.6	

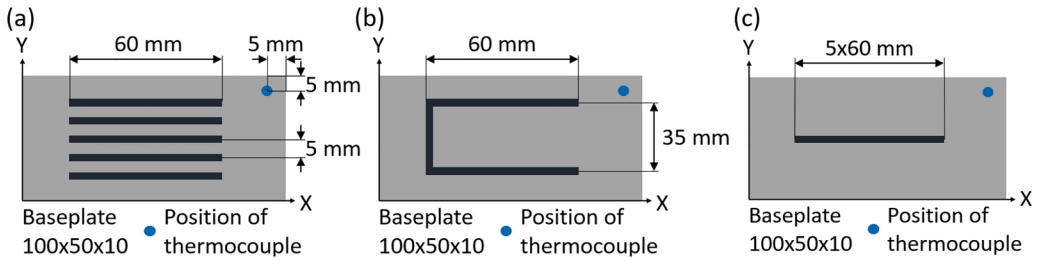

Fig. 9. Geometries and thermocouple position used for (a) Experiments 1 and 2, (b) Experiment 3, and (c) Experiment 4.

Table 3
Clads deposited in Experiments 1 and 2.

Clad	P [W]	F [mm·min^{-1}]	M [g·min^{-1}]	F_0 [mm·min^{-1}]
1.1	900	1000	16	3000
1.2	1100	1000	16	3000
1.3	1300	1000	16	3000
1.4	1100	800	16	3000
1.5	1100	1200	16	3000
2.1	900	1000	16	500
2.2	1100	1000	16	500
2.3	1300	1000	16	500
2.4	1100	800	16	500
2.5	1100	1200	16	500

On the contrary, in Experiments 3 and 4, a constant process parameter set is employed, namely that corresponding to the clad 1.2. In these cases, the objective is to study the capability of the DT to simulate the DED-L process in different deposition trajectories.

In all experiments, clads are cross-sectioned to extract three representative samples. Afterwards, a proper metallographic procedure for nickel-based alloys is applied, in which an automatic polisher from Metkon is employed for the sample grinding and polishing, the FOCIMAT 52 automatic head is mounted in a FORCIPOL 102 polisher. The microstructure is revealed using Kalling 2 reagent. Finally, the clad cross-sections are analysed using a Leica DCM-3D optical microscope.

6. Results and discussion

For developing a reliable DT, the experimental validation is one of the most important stages. For that reason, in this section, the results obtained from the DT and the experimental data are correlated.

The validation is presented in various steps. First, Experiments 1 and 2 are validated through the base plate temperature measurement, melt pool monitoring, clad dimensions, and microstructure evaluation. In the second step, Experiment 3 is performed, and the resulting geometry and temperature increase at the corners are evaluated. Finally, the height increase in Experiment 4 is measured to validate the capability of the DT to simulate multilayer depositions.

6.1. Experiments 1 and 2

6.1.1. Base plate temperature

The global model accounts for the resulting part geometry and thermal field evolution during the DED-L process. Therefore, the temperature increase during Experiments 1 and 2 is experimentally measured and compared with the results provided by the DT. The temperature values shown in Table 4 correspond to the values measured at the final instant of depositing each clad. In both experiments, the temperature of the base plate rises as the number of deposited clads increases. Moreover, in Experiment 2, where the void movement velocity is reduced, the DT is capable of predicting the lower temperatures relative to Experiment 1. In all clads, an error below 8% is obtained.

The presented Fig. 10 shows the temperature increase during Experiments 1 and 2. As shown in the numerical results, the void movement velocity has a significant effect regarding the baseplate's overall temperature. The heating rate in Experiment 1 is twice as high as in Experiment 2 while the respective temperatures for each clad are also slightly higher.

In the next Fig. 11, the thermal field evolution for Experiment 1 is shown. The position of the thermocouple is highlighted with a yellow circle, and the maximum temperatures in the color scale are limited to 100°C to highlight the desired temperature range, see Table 4 for numeric values.

6.1.2. Melt pool monitoring

The melt pool, MP, monitoring records the maximum temperature as well as the corresponding width. The experimental MP temperature measurement is realized by implementing the IR camera and the MP width by the CMOS camera in-situ, whereas in the DT, the local model is responsible for predicting these results. In Table 5, the results of the MP temperatures are listed with their corresponding errors. The MP temperature obtained in the DT, T_{MP} DT, is the mean value of the maximum temperatures recorded during the local model execution. Likewise, the MP temperature from the IR camera, T_{MP} IR, is the mean value recorded in the central position of each clad.

The obtained results present a good correlation, and the DT as well as the experimental tests present the same trend. The maximum error appears in test 2.3, which presents an 11.93% value. However, the average error for all tests is below 5%, which is an acceptable value.

After determining the maximum MP temperature, the width of the area limited by the fusion temperature is evaluated. For the MP width calculation, not only a CMOS camera is implemented, but also the algorithm developed in Python with the appropriate threshold value is executed to determine this value. In the local model, the MP width is obtained by measuring the diameter of the fusion temperature contour, which is set at 1350°C for Inconel 625, Fig. 12(a). For the same deposition parameters, which are the parameters of clad 1.4, in Fig. 12(b), the results of the CMOS camera and the subsequent thresholding based on the 250 grayscale threshold value

Table 4
The global model (GM) and experimental results for the base plate temperature.

Clad	$T_{Thermocouple}$ (°C)	T_{GM} (°C)	Error (%)
1.1	29.15	30.66	4.92
1.2	40.66	39.88	1.92
1.3	45.83	48.91	6.72
1.4	51.30	54.84	6.90
1.5	59.60	57.78	3.05
2.1	33.33	33.13	0.61
2.2	38.29	38.70	1.07
2.3	43.40	46.73	7.67
2.4	52.71	51.77	1.78
2.5	52.83	54.32	2.82

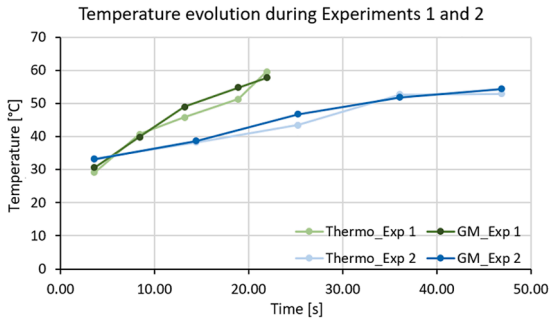

Fig. 10. The thermocouple measurements and global model (GM) temperatures during Experiments 1 and 2.

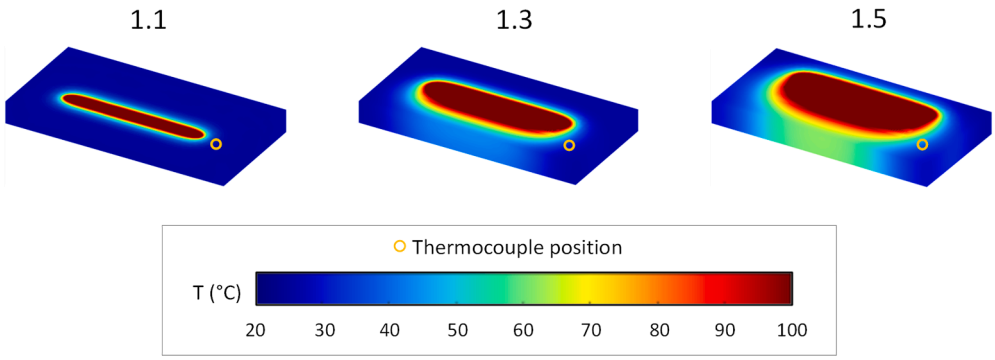

Fig. 11. The thermal field evolution in the base plate during Experiment 1.

Table 5
The model and experimental results for the MP temperature.

Clad	T_{MP} IR (°C)	T_{MP} DT (°C)	Error [%]
1.1	1835.30	1848.70	0.72
1.2	2064.10	2103.00	1.85
1.3	2174.90	2349.10	7.41
1.4	2069.30	2196.00	5.77
1.5	2004.20	2042.60	1.88
2.1	1867.30	1848.70	1.01
2.2	2014.60	2115.20	4.76
2.3	2085.60	2368.20	11.93
2.4	2040.40	2222.60	8.20
2.5	2014.40	2070.10	2.69

are provided.

The numerical values of the experimental tests and the DT are listed in Table 6, where a 4% average error is obtained between the monitored signal ($Ø_M$) and the DT results ($Ø_{DT}$).

6.1.3. Clad dimensions

The clad dimensions of the DT are directly compared with the experimental results obtained after the metallographic inspection. The clad dimensions are exclusively calculated in the local model, where the clad height (H_{DT}) and width (W_{DT}) are obtained considering the nodes displacement. Hereafter, in Table 7, the simulated clad height and width are compared with the experimental values, H_E and W_E, respectively.

The results indicate that the maximum error is around 11% for the height and 9% for the width. At this point, it is noticed that the employed minimum element size in the local model restricts the resolution of the DT clad width. In the present study, a 0.2 mm minimum element size is employed, and as can be seen in Table 7, the error is practically confined by this value. On the contrary, regarding the clad height, the numerical differences between the simulated and the experimental values are rather low, with a 50 μm average deviation and a maximum value of 100 μm.

The clad generation in the local model is represented in Fig. 13(a), where the displaced nodes are highlighted with black dots. In Fig. 13(b), the cross-section of the clad 2.5 is displayed. As can be seen, the width and height given by the DT are slightly larger than the

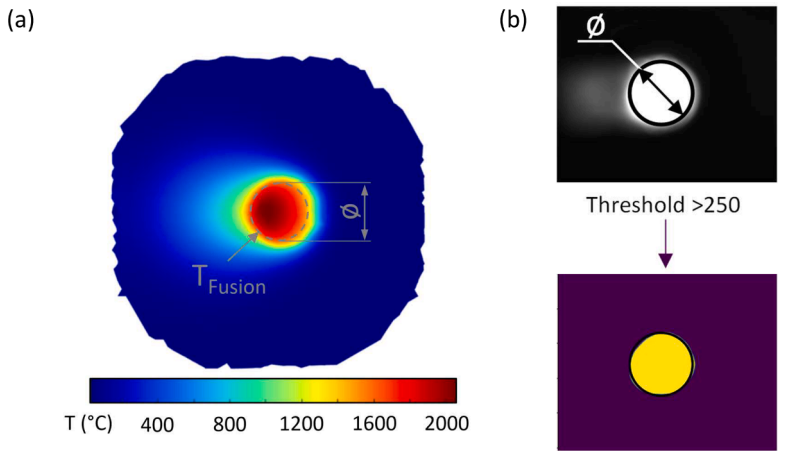

Fig. 12. MP width (Clad 1.4): (a) results given by the local model and (b) results obtained from the coaxial camera.

Table 6
The monitored and simulated results for melt pool width.

Clad	$Ø_M$ [mm]	$Ø_{DT}$ [mm]	Error [%]
1.1	1.97	2.03	3.05
1.2	2.15	2.05	4.83
1.3	2.28	2.13	6.94
1.4	2.22	2.13	4.18
1.5	2.17	2.08	4.33
2.1	1.99	2.03	2.07
2.2	2.13	2.05	3.85
2.3	2.27	2.13	6.47
2.4	2.21	2.13	3.71
2.5	2.10	2.08	0.96

Table 7
The metallography and DT results for the clad dimensions.

Clad	H_E [mm]	H_{DT} [mm]	$Error_H$ [%]	W_E [mm]	W_{DT} [mm]	$Error_W$ [%]
1.1	0.78	0.83	6.35	1.86	2.03	8.61
1.2	0.78	0.83	6.31	1.90	2.03	6.30
1.3	0.81	0.89	8.92	2.06	2.03	1.38
1.4	0.95	1.04	9.09	2.01	2.03	0.88
1.5	0.67	0.69	2.96	1.91	2.03	5.76
2.1	0.77	0.83	7.10	1.86	2.03	8.61
2.2	0.78	0.83	6.39	1.95	2.03	4.01
2.3	0.79	0.89	11.15	2.04	2.03	0.44
2.4	0.93	1.04	10.54	2.03	2.03	0.23
2.5	0.69	0.69	1.01	1.90	2.03	6.58

experimental ones.

6.1.4. Microstructure analysis

The cooling rate, CR, is an important factor for the DED-L manufactured parts due to the considerable changes the microstructure can present. For that reason, apart from evaluating the clad dimensions with the cross-section metallography, the dendrite arm spacing is also measured. Precisely, the secondary dendrite arm spacing (SDAS) is evaluated because it represents the thermal gradients and the solidification process between the liquidus and solidus temperatures [48]. Several investigations show that there is an empirical relationship between the CR and the SDAS depending on the material [49,50]. Therefore, the following empirical equation (Eq. (14)) is implemented for Inconel 625 where *CR* is the cooling rate obtained from the DT (Fig. 14(a)), and *c* and *n* are constant values specified by the material, being 23.31 and -0.342 respectively [49].

$$SDAS(\mu m) = c \cdot CR^n \tag{14}$$

The experimental measurements of the SDAS (λ_2) are realized by a Leica DCM-3D microscope. Hereafter, an example of how the

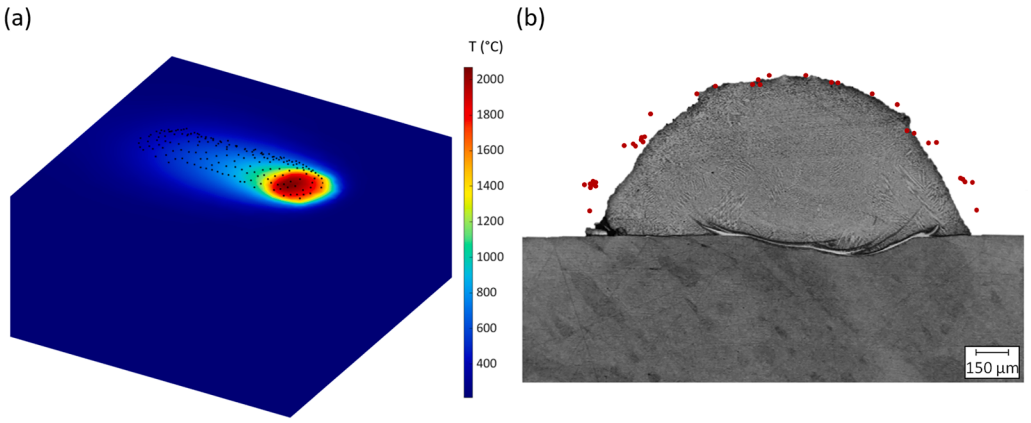

Fig. 13. Clad 2.5 results: (a) Thermal field and clad generation results of the local model, and (b) superimposition of the results obtained by the DT (red points) and the corresponding cross-section.

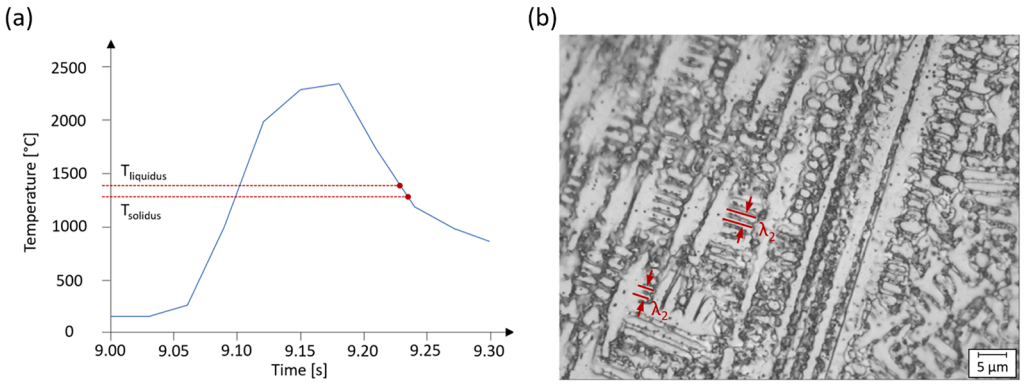

Fig. 14. (a) simulated CR for the SDAS calculation of clad 2.3 and (b) SDAS representation in the metallography of clad 2.3.

SDAS dimensions are measured is shown in Fig. 14(b). To ensure a real trend, 16 individual measurements are realized for each clad, and afterwards, the mean values are employed for the following validation.

The SDAS calculated by the empirical equation with the CR obtained from the DT, $SDAS_{DT}$, are listed and compared with the experimental measurements, $SDAS_E$, in Table 8.

Considering the assumptions implemented in the model, the maximum error of 0.36 µm is satisfactory. Moreover, an average measurement discrepancy of 0.18 µm appears to be highly precise.

6.2. *Experiment 3*

Once the validity of the DT for single clad simulation is ensured, a U-Type structure manufacturing is discussed to account for the sharp edge effect. The DT results are collected in strategic points decided by the DT user. For this experiment, five points are evaluated,

Table 8
The metallography and modelled results for the SDAS.

Clad	CR (°C·s^{-1})	$SDAS_E$ [µm]	$SDAS_{DT}$ [µm]	Error [µm]
1.1	2000	1.81	1.73	0.08
1.2	2000	1.83	1.73	0.10
1.3	1000	2.07	1.73	0.34
1.4	800	2.22	2.37	0.15
1.5	2400	1.94	1.63	0.31
2.1	2000	1.78	1.73	0.05
2.2	2000	1.83	1.73	0.10
2.3	1000	2.09	1.73	0.36
2.4	800	2.07	2.37	0.30
2.5	2400	1.57	1.63	0.06

which are presented in Fig. 15(a).

The base plate temperature evolution during the DED-L process is shown in Table 9 and presents little error when compared with the experimental values collected from the thermocouple measurements. Regarding the MP temperature values, due to the position of the IR camera, the accuracy of the results is only assured in the center of the plate. This is the reason for validating the model only at points 3.1 and 3.5 and not providing the values at 3.2, 3.3, and 3.4.

The resultant geometry of the global model is presented in Fig. 15(b), where the employed Delaunay triangularization results in a little chamfer on the internal part of the sharp edge. Moreover, the temperature field during the clad deposition is also shown in Fig. 15 (c) at three different evaluation points. The black dots represent the displaced nodes and, therefore, the deposited clad shape.

6.3. *Experiment 4*

The aim of Experiment 4 is to validate the multilayer deposition capability of the DT, because as the wall height raises, it is likely that the accumulated height error increases subsequently. The heat accumulation in the base plate during the wall deposition is a fact that directly affects the DED-L process. In Table 10, the base plate experimental and modelled temperatures are listed, as well as the error, which is, in all cases below 8%. Consequently, it can be concluded that the DT can quite accurately predict the heat accumulation during the successive clad deposition.

Regarding the MP temperatures, the DT shows an increasing temperature value, whereas the IR camera provides an almost constant temperature value. Therefore, the obtained error rises from the 1.29% value obtained in the first clad to 5.62% in the fifth. This deviation could be generated by the omission of the melt pool dynamics in the local model, which tends to lower the maximum temperatures. Nevertheless, the error is considered admissible and the DT valid.

For the five clads in Experiment 4, it is necessary to notice that from the first layer onwards, the subsequent clads are not deposited on a flat surface but on the previously deposited clad. Fig. 16(a) depicts this effect during the deposition of clad 4.3. Lastly, in Fig. 16 (b), the cross-section of the five clads is shown over the geometry predicted by the global model of the DT. The height prediction error is below 7%, which confirms the accuracy of the DT and the validity of employing a multiscale model for DED-L simulation.

7. Conclusions

In the present research, a multiscale DT has been developed based on coupling a local and a global model, which enables to approach the simulation of the DED-L process at a reasonable computational cost, but without compromising the accuracy of the results. The DT has been validated through experimental testing, where a monitoring framework has been implemented in a BeAM Modulo 400 DED-L machine to measure the melt pool diameter and maximum temperatures in-situ. Those measurements have been compared with the results of the DT, and the main conclusions are as follows:

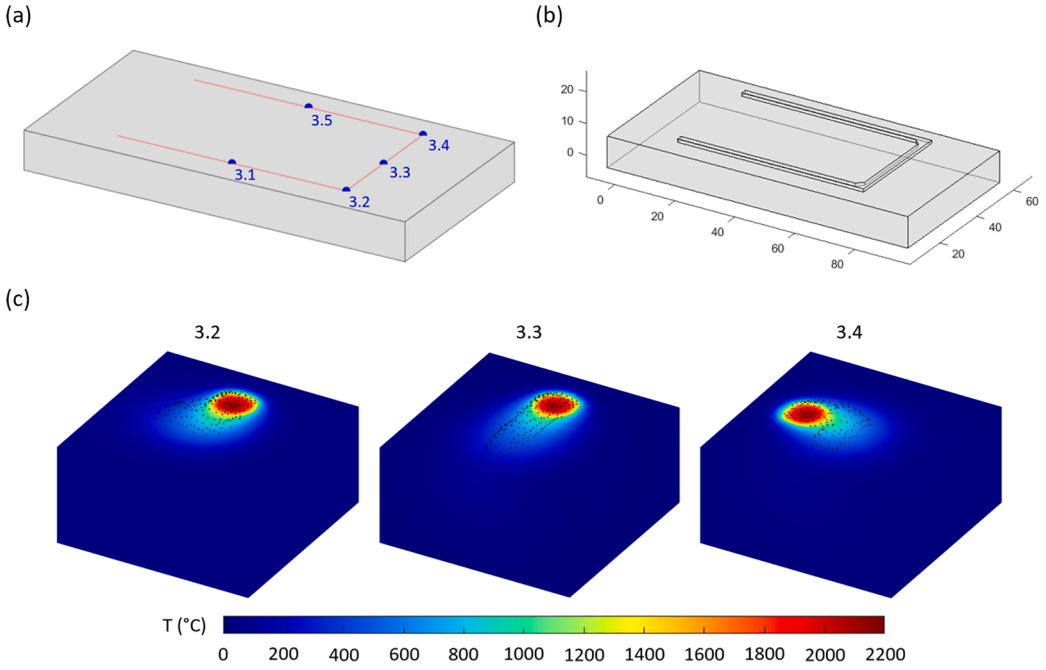

Fig. 15. DT results for Experiment 3: (a) Evaluation points of Experiment 3, (b) the global model resulting geometry, (c) local model temperature field and clad in points 3.2, 3.3 and 3.4.

Table 9
DT and experimental results for the thermocouple and MP temperatures in Experiment 3.

Point	$T_{Thermocouple}$ (°C)	T_{GM} (°C)	Error (%)	T_{MP} IR camera (°C)	T_{MP} DT (°C)	Error [%]
3.1	30.90	27.84	9.91	1972.55	2129.70	7.37
3.3	30.16	31.26	3.66	-	2138.5	-
3.5	37.49	34.92	6.86	2036.38	2132.00	4.49

Table 10
The model and experimental results for the thermocouple temperature in Experiment 4.

Clad	$T_{Thermocouple}$ (°C)	$T_{Global\ Model}$ (°C)	Error (%)	T_{MP} IR (°C)	T_{MP} DT (°C)	Error [%]	H_E [mm]	H_{DT} [mm]	Error [%]
4.1	33.17	31.85	3.97	2047.06	2021.30	1.29	-	-	-
4.2	39.63	37.24	6.03	2045.00	2098. 80	2.53	-	-	-
4.3	41.55	44.77	7.76	2008.95	2086.30	3.69	-	-	-
4.4	48.46	50.90	5.04	2039.25	2134.10	4.44	-	-	-
4.5	54.31	57.07	5.07	2043.43	2165.60	5.62	3.15	3.38	6.88

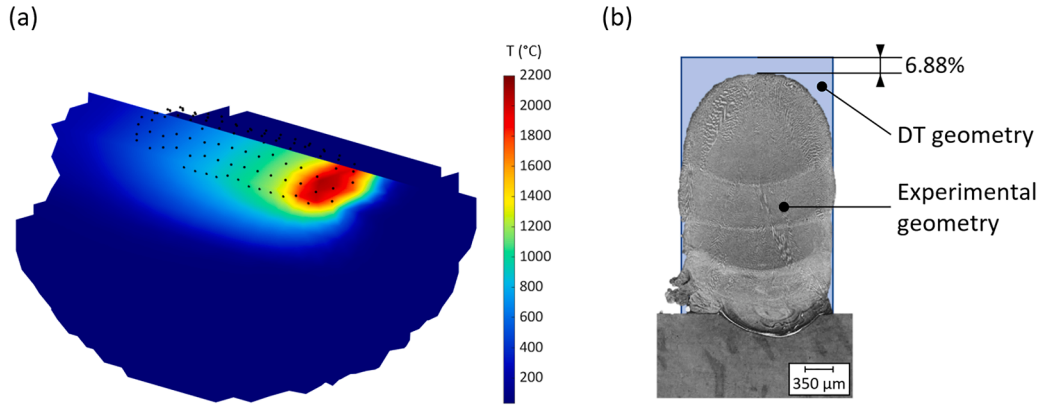

Fig. 16. Experiment 4: (a) simulation of the clad 4.3 and (b) comparison between the experimental and DT results.

- The multiscale approach is applicable for DTs aimed at modelling the DED-L process. The local model can accurately predict the clad dimensions, with an error below 11.2% and maximum temperatures with a maximum deviation of 11.9%. The average error for the clad dimensions and the maximum temperature amounted to 4% and 4.62%, respectively.
- Moreover, the small size of the local model enables to increase the mesh density and simulate the fast-cooling rates typical in DED-L. The resulting SDAS is calculated based on the cooling rate, and an average error of 0.18 µm has been obtained in Experiments 1 and 2.
- The global model simulates the heating of the baseplate during the deposition process. This feature is impossible to obtain with local models or models of small dimensions, and it is necessary for multiple clad simulations, where the deposition conditions evolve during the printing. The mean temperature errors obtained between the experimental thermocouple measurements and the global model are 4.70 %, 2.79 %, 6.81 %, and 5.56 % for Experiments 1-4, respectively.
- In Experiments 3 and 4, abrupt direction changes and multiple clad overlap situations have been simulated. In all cases, the DT behaves correctly, and high resemblance with the experimental tests is obtained. This ensures the validity of the DT for larger scale applications as far as the predictions of melt pool dimensions, with a mean error of 4-5%, and temperatures, with a mean error of 7%, are concerned.

Future research will focus on applying the DT to more complex use cases such as larger geometries, other materials, and multi-material parts. The utilized partial differential equations will also be integrated into the loss function of a machine learning model to evaluate the capabilities of a physics-informed neural network for process parameter prediction.

CRediT authorship contribution statement

Sebastian Hartmann: Conceptualization, Data curation, Formal analysis, Investigation, Methodology, Project administration, Resources, Software, Validation, Visualization, Writing – original draft, Writing – review & editing. **Oihane Murua:** Conceptualization, Data curation, Formal analysis, Investigation, Methodology, Project administration, Resources, Software, Validation, Visualization, Writing – original draft, Writing – review & editing. **Jon Iñaki Arrizubieta:** Conceptualization, Funding acquisition,

Investigation, Methodology, Resources, Software, Supervision, Writing – original draft, Writing – review & editing. **Aitzol Lamikiz:** Funding acquisition, Supervision, Writing – review & editing. **Peter Mayr:** Supervision, Writing – review & editing.

Declaration of Competing Interest

None.

Data availability

The data that has been used is confidential.

Acknowledgements

Grant TED2021-130543B-I00 funded by the MCIN/AEI/10.13039/501100011033 and the European Union NextGenerationEU/PRTR.

Supplementary materials

Supplementary material associated with this article can be found, in the online version, at doi:10.1016/j.simpat.2023.102881.

Appendix

Monitoring framework

Sensor name	Frequency	Process parameters	Source
Machine data	500 Hz	- X, Y, Z - Laser power - Speed	Edge IPC
Thermocouple	500 Hz	- Temperature at constant position	Edge IPC
Melt pool camera	88 Hz	- Melt pool width	Windows IPC
IR camera	80 Hz	- Max. melt pool temperature	Windows IPC

References

[1] H.G. Lemu, On opportunities and limitations of additive manufacturing technology for industry 4.0 era, in: K. Wang, Y. Wang, J.O. Strandhagen, T. Yu (Eds.), Lecture Notes in Electrical Engineering, Advanced Manufacturing and Automation VIII, Springer Singapore, Singapore, 2019, pp. 106–113.
[2] D.-G. Ahn, Directed Energy Deposition (DED) process: state of the art, Int. J. Precis. Eng. Manuf.-Green Tech. 8 (2) (2021) 703–742, https://doi.org/10.1007/s40684-020-00302-7.
[3] G. Gong, J. Yi, Y. Chi, Z. Zhao, Z. Wang, G. Xia, X. Du, H. Tian, H. Yu, C. Chen, Research status of laser additive manufacturing for metal: a review, J. Mater. Res. Technol. 15 (2021) 855–884, https://doi.org/10.1016/j.jmrt.2021.08.050.
[4] Additive manufacturing for aerospace - Process characteristics and performance - Part 2: Directed energy deposition using wire and arc, ISO/ASTM DIS 52943-2, International Organization for Standardization (ISO), 2023. Geneva, Switzerland[Online]. Available, https://www.iso.org/standard/75761.html (Accessed: 06 December 2023).
[5] D. Svetlizky, M. Das, B. Zheng, A.L. Vyatskikh, S. Bose, A. Bandyopadhyay, J.M. Schoenung, E.J. Lavernia, N. Eliaz, Directed energy deposition (DED) additive manufacturing: physical characteristics, defects, challenges and applications, Mater. Today 49 (2021) 271–295, https://doi.org/10.1016/j.mattod.2021.03.020.
[6] D.S. Ertay, M.A. Naiel, M. Vlasea, P. Fieguth, Process performance evaluation and classification via in-situ melt pool monitoring in directed energy deposition, CIRP J. Manuf. Sci. Technol. 35 (2021) 298–314, https://doi.org/10.1016/j.cirpj.2021.06.015.
[7] Z. Jin, Z. Zhang, K. Demir, G.X. Gu, Machine learning for advanced additive manufacturing, Matter 3 (5) (2020) 1541–1556, https://doi.org/10.1016/j.matt.2020.08.023.
[8] A.P. Markopoulos, Cutting mechanics and analytical modeling. SpringerBriefs in Applied Sciences and Technology, Finite Element Method in Machining Processes, A.P. Markopoulos, Ed, Springer London, London, 2013, pp. 11–27.
[9] T. DebRoy, W. Zhang, J. Turner, S.S. Babu, Building Digital Twins of 3D printing machines, Scr. Mater. 135 (2017) 119–124, https://doi.org/10.1016/j.scriptamat.2016.12.005.
[10] A. Gaikwad, R. Yavari, M. Montazeri, K. Cole, L. Bian, P. Rao, Toward the Digital Twin of additive manufacturing: integrating thermal simulations, sensing, and analytics to detect process faults, IISE Trans. 52 (11) (2020) 1204–1217, https://doi.org/10.1080/24725854.2019.1701753.
[11] D.R. Gunasegaram, A.B. Murphy, A. Barnard, T. DebRoy, M.J. Matthews, L. Ladani, D. Gu, Towards developing multiscale-multiphysics models and their surrogates for Digital Twins of metal additive manufacturing, Addit. Manuf. 46 (2021) 102089, https://doi.org/10.1016/j.addma.2021.102089.
[12] T. Mukherjee, T. DebRoy, A Digital Twin for rapid qualification of 3D printed metallic components, Appl. Mater. Today 14 (2019) 59–65, https://doi.org/10.1016/j.apmt.2018.11.003.

[13] R.T. Reisch, T. Hauser, B. Lutz, A. Tsakpinis, D. Winter, T. Kamps, A. Knoll, Context awareness in process monitoring of additive manufacturing using a Digital Twin, Int. J. Adv. Manuf. Technol. (2022), https://doi.org/10.1007/s00170-021-08636-5.

[14] F. Hermann, B. Chen, G. Ghasemi, V. Stegmaier, T. Ackermann, P. Reimann, S. Vogt, T. Graf, M. Weyrich, A Digital Twin approach for the prediction of the geometry of single tracks produced by laser metal deposition, Proc. CIRP 107 (2022) 83–88, https://doi.org/10.1016/j.procir.2022.04.014.

[15] J.V. Soares do Amaral, J.A.B. Montevechi, R.d.C. Miranda, W.T.d.S. Junior, Metamodel-based simulation optimization: a systematic literature review, Simul. Modell. Pract. Theory 114 (2022) 102403, https://doi.org/10.1016/j.simpat.2021.102403.

[16] J.I. Arrizubieta, A. Lamikiz, F. Klocke, S. Martínez, K. Arntz, E. Ukar, Evaluation of the relevance of melt pool dynamics in Laser Material Deposition process modeling, Int. J. Heat Mass Transfer 115 (2017) 80–91, https://doi.org/10.1016/j.ijheatmasstransfer.2017.07.011.

[17] Y. Ling, J. Ni, J. Antonissen, H. Ben Hamouda, J. Vande Voorde, M. Abdel Wahab, Numerical prediction of microstructure and hardness for low carbon steel wire arc additive manufacturing components, Simul. Modell. Pract. Theory 122 (2023) 102664, https://doi.org/10.1016/j.simpat.2022.102664.

[18] A. Riensche, J. Severson, R. Yavari, N.L. Piercy, K.D. Cole, P. Rao, Thermal modeling of directed energy deposition additive manufacturing using graph theory, Rapid Prototyping J. (2022), https://doi.org/10.1108/RPJ-07-2021-0184.

[19] Z. Feng, J. Wang, X. Zhou, C. Zhai, Y. Ma, Robust optimization for functional multiresponse in 3D printing process, Simul. Modell. Pract. Theory 126 (2023) 102774, https://doi.org/10.1016/j.simpat.2023.102774.

[20] D. Weisz-Patrault, Fast simulation of temperature and phase transitions in directed energy deposition additive manufacturing, Addit. Manuf. 31 (2020) 100990, https://doi.org/10.1016/j.addma.2019.100990.

[21] W. Yan, S. Lin, O.L. Kafka, C. Yu, Z. Liu, Y. Lian, S. Wolff, Cao J, G.J. Wagner, W.K. Liu, Modeling process-structure-property relationships for additive manufacturing, Front. Mech. Eng. 13 (4) (2018) 482–492, https://doi.org/10.1007/s11465-018-0505-y.

[22] Z. Tang, W. Liu, Y. Wang, K.M. Saleheen, Z. Liu, S. Peng, Z. Zhang, H. Zhang, A review on in situ monitoring technology for directed energy deposition of metals, Int. J. Adv. Manuf. Technol. 108 (2020) 3437–3463, https://doi.org/10.1007/s00170-020-05569-3, 11-12.

[23] W. Liu, Z. Tang, X.-Y. Liu, H.-J. Wang, H. Zhang, A review on in-situ monitoring and adaptive control technology for laser cladding remanufacturing, Proc. CIRP 61 (2017) 235–240, https://doi.org/10.1016/j.procir.2016.11.217, a.

[24] W. He, W. Shi, J. Li, H. Xie, In-situ monitoring and deformation characterization by optical techniques; part I: laser-aided direct metal deposition for additive manufacturing, Opt. Lasers Eng. 122 (2019) 74–88, https://doi.org/10.1016/j.optlaseng.2019.05.020.

[25] A.P. Markopoulos, N.E. Karkalos, E.-L. Papazoglou, Meshless methods for the simulation of machining and micro-machining: a review, Arch. Comput. Methods Eng. 27 (3) (2020) 831–853, https://doi.org/10.1007/s11831-019-09333-z.

[26] F. Wirth, S. Arpagaus, K. Wegener, Analysis of melt pool dynamics in laser cladding and direct metal deposition by automated high-speed camera image evaluation, Addit. Manuf. 21 (2018) 369–382, https://doi.org/10.1016/j.addma.2018.03.025.

[27] A. Aggarwal, A. Chouhan, S. Patel, D.K. Yadav, A. Kumar, A.R. Vinod, K.G. Prashanth, N.P. Gurao, Role of impinging powder particles on melt pool hydrodynamics, thermal behaviour and microstructure in laser-assisted DED process: a particle-scale DEM – CFD – CA approach, Int. J. Heat Mass Transfer 158 (2020) 119989, https://doi.org/10.1016/j.ijheatmasstransfer.2020.119989.

[28] E. Kundakcıoğlu, I. Lazoglu, Ö. Poyraz, E. Yasa, N. Cizicioğlu, Thermal and molten pool model in selective laser melting process of Inconel 625, Int. J. Adv. Manuf. Technol. 95 (9-12) (2018) 3977–3984, https://doi.org/10.1007/s00170-017-1489-1.

[29] H. Ge, H. Xu, J. Wang, J. Li, J. Yao, Investigation on composition distribution of dissimilar laser cladding process using a three-phase model, Int. J. Heat Mass Transfer 170 (2021) 120975, https://doi.org/10.1016/j.ijheatmasstransfer.2021.120975.

[30] C. Sainte-Catherine, M. Jeandin, D. Kechemair, J.-P. Ricaud, L. Sabatier, Study of dynamic absorptivity at 10.6 μm (CO 2) and 1.06 μm (Nd-YAG) wavelengths as a function of temperature, J. Phys. IV France 01 (C7) (1991), https://doi.org/10.1051/jp4:1991741. C7-151-C7-157.

[31] T. DebRoy, H.L. Wei, J.S. Zuback, T. Mukherjee, J.W. Elmer, J.O. Milewski, A.M. Beese, A. Wilson-Heid, A. De, W. Zhang, Additive manufacturing of metallic components – process, structure and properties, Prog. Mater. Sci. 92 (2018) 112–224, https://doi.org/10.1016/j.pmatsci.2017.10.001.

[32] D.L. Bourell, W. Frazier, H. Kuhn, M. Seifi, Additive Manufacturing Processes. Materials Park, ASM International, Ohio, 2020.

[33] Z. Liu, X. Wang, T. Wuest, H. Zhang, Modeling and experimental analysis of energy attenuation and partitioning during laser based direct energy deposition, Proc. Manuf. 48 (2020) 656–662, https://doi.org/10.1016/j.promfg.2020.05.094, b.

[34] F. Lia, J. Park, J. Tressler, R. Martukanitz, Partitioning of laser energy during directed energy deposition, Addit. Manuf. 18 (2017) 31–39, https://doi.org/10.1016/j.addma.2017.08.012.

[35] M. Kubiak, W. Piekarska, S. Stano, Modelling of laser beam heat source based on experimental research of Yb:YAG laser power distribution, Int. J. Heat Mass Transfer 83 (2015) 679–689, https://doi.org/10.1016/j.ijheatmasstransfer.2014.12.052.

[36] J.C. Heigel, P. Michaleris, E.W. Reutzel, Thermo-mechanical model development and validation of directed energy deposition additive manufacturing of Ti–6Al–4V,", Addit. Manuf. 5 (2015) 9–19, https://doi.org/10.1016/j.addma.2014.10.003.

[37] Optris GmbH, *optris PI 05M: Technical data.* [Online]. Available: https://www.optris.com/en/product/infrared-cameras/pi-series/pi-05m/ (Accessed: 06 December 2023).

[38] O. Murua, J.I. Arrizubieta, A. Lamikiz, L. Galdos, Laser welding for stamping blank reinforcement: signal monitoring for digital certification, Proc. CIRP 111 (2022) 536–540, https://doi.org/10.1016/j.procir.2022.08.086.

[39] A. Oliveira, A. Avrit, M. Gradeck, Thermocouple response time estimation and temperature signal correction for an accurate heat flux calculation in inverse heat conduction problems, Int. J. Heat Mass Transfer 185 (2022) 122398, https://doi.org/10.1016/j.ijheatmasstransfer.2021.122398.

[40] M. Khanzadeh, S. Chowdhury, M. Marufuzzaman, M.A. Tschopp, L. Bian, Porosity prediction: supervised-learning of thermal history for direct laser deposition, J. Manuf. Syst. 47 (2018) 69–82, https://doi.org/10.1016/j.jmsy.2018.04.001.

[41] thyssenkrup Materials (UK) Ltd., Stainless steel 304 1.4301. [Online]. Available: https://www.thyssenkrupp-materials.co.uk/stainless-steel-304-14301.html (Accessed: 06 December 2023).

[42] Oerlikon Metco, *Material product data sheet: nickel – chromium – molybdenum powder for additive manufacturing.* [Online]. Available: https://www.oerlikon.com/ecoma/files/DSM-0318.0_AM_625_Ni_Alloy.pdf?download=true (Accessed: 06 December 2023).

[43] H. Arora, R. Singh, G.S. Brar, Numerical simulation on residual stresses of stainless steel SS-304 thin welded pipe, Meas. Control 53 (7-8) (2020) 1183–1193, https://doi.org/10.1177/0020294020917173.

[44] I. Tlili, D. Baleanu, S.Mohammad Sajadi, F. Ghaemi, M.A. Fagiry, Numerical and experimental analysis of temperature distribution and melt flow in fiber laser welding of Inconel 625, Int. J. Adv. Manuf. Technol. 121 (1-2) (2022) 765–784, https://doi.org/10.1007/s00170-022-09329-3.

[45] R.H. Bogaard, Thermal conductivity of selected stainless steels, in: T. Ashworth, D.R. Smith (Eds.), Thermal Conductivity 18, Springer US, Boston, MA, 1985, pp. 175–185.

[46] Haynes International, *Haynes 625 alloy.* Available: https://www.haynesintl.com/alloys/alloy-portfolio_/High-temperature-Alloys/HAYNES625Alloy/physical-properties (Accessed: 06 December 2023).

[47] S. Baraldo, A. Vandone, A. Valente, E. Carpanzano, Vision-based control for track geometry optimization of complex AM motion profiles by on-line laser power modulation, Proc. CIRP 95 (2020) 78–82, https://doi.org/10.1016/j.procir.2020.01.167.

[48] Z. Gan, Y. Lian, S.E. Lin, K.K. Jones, W.K. Liu, G.J. Wagner, Benchmark study of thermal behavior, surface topography, and dendritic microstructure in selective laser melting of Inconel 625, Integr. Mater. Manuf. Innov. 8 (2) (2019) 178–193, https://doi.org/10.1007/s40192-019-00130-x.

[49] F. Lia, J.Z. Park, J.S. Keist, S. Joshi, R.P. Martukanitz, Thermal and microstructural analysis of laser-based directed energy deposition for Ti-6Al-4V and Inconel 625 deposits, Mater. Sci. Eng.: A 717 (2018) 1–10, https://doi.org/10.1016/j.msea.2018.01.060.

[50] J. Tinoco, H. Fredriksson, Solidification of a modified Inconel 625 alloy under different cooling rates, High Temp. Mater. Processes 23 (1) (2004) 13–24, https://doi.org/10.1515/HTMP.2004.23.1.13.